DOI: https://doi.org/10.53256/COSE_250104

MODELING OF DIFFRACTION AROUND BREAKWATERS USING THE THREE-DIMENSIONAL NON-HYDROSTATIC SOLVER REEF3D::NHFLOW

Thomas Becker[a,*], Widar Weizhi Wang[a] and Hans Bihs[a]
[a]*Norwegian University of Science and Technology (NTNU), Norway, thomas.becker@ntnu.no, widar.w.wang@ntnu.no, hans.bihs@ntnu.no*

[*]*Corresponding author*

ABSTRACT: The effectiveness of breakwaters in attenuating wave energy is largely determined by the wave heights attained leeward of the structures relative to the incoming waves. To simulate diffraction around breakwaters—both as an isolated phenomenon and under realistic site conditions—the phase-resolving, three-dimensional, non-hydrostatic model REEF3D::NHFLOW is presented. The model is validated against the analytical solution for monochromatic wave diffraction around a fully rigid, slender, semi-infinite breakwater derived by Penney and Price (1952), based on the classical Sommerfeld solution. Validation is performed through direct comparison of the simulated diffraction coefficients in the lee of the structure and their spatial distribution with the analytical reference solution. In addition, the model is applied to simulate extreme wave conditions propagating into Sirevåg Harbour, Norway, which is protected by a large breakwater. The resulting wave characteristics are compared with phase-averaged wave propagation computed using the spectral wave model SWAN, which inherently cannot accurately resolve diffraction processes. The predicted diffraction coefficients obtained with NHFLOW show good agreement with the Sommerfeld solution, yielding a root-mean-square error of 0.012 relative to the analytical diffraction coefficients. In the Sirevåg Harbour case, NHFLOW predicts greater energy dissipation as waves propagate toward the breakwater opening compared with the spectral model. However, significant wave heights inside the harbour basins are notably higher in NHFLOW, indicating that more wave energy is diffracted into these sheltered areas. This suggests that the phase-resolving model provides more physically realistic and potentially more conservative estimates of wave conditions within protected harbour zones.

KEYWORDS: Coastal hydrodynamics, harbor design, Sommerfeld solution, computational fluid dynamics

1 INTRODUCTION

Diffraction describes the propagation of wave energy perpendicular to the principal direction of wave travel, toward regions of lower wave energy. This process results in the bending of wave fronts into sheltered areas, for example into the lee of breakwaters. Particularly within harbour basins, diffraction is a critical mechanism influencing wave penetration, spatial energy redistribution, and wave attenuation (cf. Dean and Dalrymple, 1991; US Army Corps of Engineers, 2008).

Early analytical descriptions of diffraction were developed in optics, where wave crests were conceptualised as arrays of spherical point sources, as proposed by Huygens (1690) and later refined to account for directionality by Fresnel (1819). Subsequent formulations by Sommerfeld (1896), for diffraction by a semi-infinite screen, and by Sieger (1908), followed by Morse and Rubenstein (1938), for diffraction through slits in infinite screens, employed geometric expansions of Maxwell's equations to derive analytical solutions for diffraction coefficients.

These theoretical approaches were later adapted to water waves by Penney and Price (1952) and Carr and Stelzriede (1952), who applied analogous solution techniques to the linearised potential flow equations governing surface gravity waves. However, these analytical solutions are restricted to waves of small steepness propagating over a horizontal bed with constant still-water depth. In addition, they assume idealised, infinitely thin, fully reflective breakwaters.

In the present study, the water-wave Sommerfeld solution formulated by Penney and Price (1952)

is used to validate diffracted wave fields simulated with the three-dimensional, non-hydrostatic numerical model REEF3D::NHFLOW.

In practical applications, diffraction around breakwaters is rarely an isolated phenomenon and typically occurs in conjunction with other wave transformation processes. Wave conditions in the lee of breakwaters depend not only on the incident sea state, but also on local bathymetry, structural geometry, and additional site-specific parameters. To account for this complexity, the performance of breakwater designs may be assessed through scaled physical model tests or through high-fidelity numerical simulations capable of resolving dispersive wave characteristics and nonlinear wave transformation processes (cf. Goda, 2000; US Army Corps of Engineers, 2008). In this study, NHFLOW is applied to simulate an extreme sea state at Sirevåg Harbour in Rogaland, Norway. The resulting wave conditions inside the harbour are compared with those obtained from an equivalent simulation using the spectral wave model SWAN.

2 THEORY

2.1 *The Sommerfeld Solution for Water Waves*

The Sommerfeld solution for water waves was derived by Penney and Price (1952) for an infinitely thin, semi-infinite breakwater, with its tip located at $x = 0$and $y = 0$in a local horizontal coordinate system, as illustrated in Fig. 1. The diffraction coefficient, $k_{diff} = H_{diff} / H_{inc}$, relates the incident wave height H_{inc} to the diffracted wave height H_{diff} at an arbitrary point in the domain. The coefficient is evaluated based on the polar coordinates of the point of interest, for a given wave incidence angle and wavelength L.

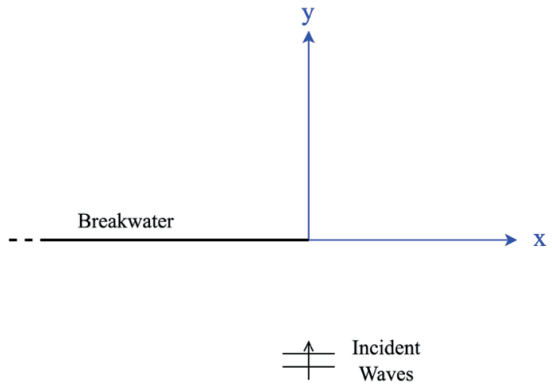

Figure 1. Geometric configuration used in the Sommerfeld solution (breakwater at $x \leq 0$; perpendicular wave incidence)

The solution is obtained by imposing additional no-flow and constant-pressure boundary conditions at the breakwater onto the classical Airy wave solution. The resulting boundary-value problem becomes tractable through the application of Sommerfeld's (1896) method, which extends the solution space using a Riemann surface formulation. The Sommerfeld solution accounts for incident and reflected wave components, their diffraction around the breakwater tip, and the interference patterns arising from their superposition in different regions of the spatial domain.

An excerpt of the solution in the lee of the breakwater ($y \geq 0$) is shown in Fig. 2.

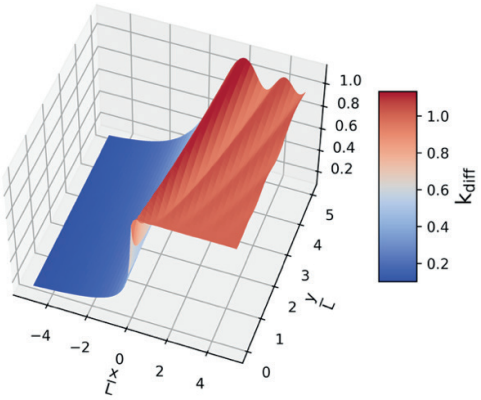

Figure 2. Sommerfeld solution for the diffraction coefficient k_{diff} in the lee of a semi-infinite breakwater located at $y = 0$and $x \leq 0$ (coordinates normalised by the wavelength L) for perpendicular wave incidence

2.2 *REEF3D::NHFLOW*

NHFLOW (Bihs et al., 2024, Bihs and Wang, 2025) is one of four numerical models currently available within the open-source software framework REEF3D. Its development was preceded by a high-resolution Navier–Stokes model (Bihs et al., 2016), a non-hydrostatic shallow water equation solver (Wang et al., 2020), and a fully nonlinear potential flow model (Wang et al., 2022), each designed for different applications in water wave modelling. NHFLOW combines high-fidelity flow-field computation with large-scale applicability across a wide range of water depths and complex bathymetries.

NHFLOW solves the three-dimensional Euler equations for mass and momentum conservation (Eqs. 1 and 2), where u denotes the velocity vector, h the water depth, ρ the water density, p the pressure, and g the gravitational acceleration. Viscous terms may be included in the momentum equation to extend the formulation to the full Navier–Stokes equations; however, they are not considered in the present study.

$$\frac{\partial u_i}{\partial x_i} = 0 \quad (1)$$

$$\frac{\partial hu_i}{\partial t} + u_j \frac{\partial hu_i}{\partial x_j} + \frac{h}{\rho}\frac{\partial p_i}{\partial x_i} + hg_i = 0 \quad (2)$$

The non-hydrostatic pressure field is computed using a pressure-correction method.
The governing equations are solved for the water phase on a rectilinear grid. The vertical coordinate z, defined over an arbitrarily shaped seabed, is transformed into a terrain-following σ-coordinate system, with relative spacing between the seabed $z_b$and the free surface $d + \eta$(where $d$is the still water depth and η the free-surface elevation), as defined in Eq. 3. This transformation is updated at each time step after the free-surface position in the Cartesian coordinate system $(d + \eta)$ is advanced through horizontal mass-flux integration over the water column.

$$\sigma = \frac{z - z_b}{d + \eta - z_b} \quad (3)$$

For local conservation and shock-capturing capability, a finite-difference method with a Godunov-type scheme is employed, incorporating an approximate Riemann solver and WENO flux reconstruction (Jiang and Shu, 1996). Time integration is performed using adaptive time stepping based on a prescribed Courant–Friedrichs–Lewy (CFL) number and a second-order total variation diminishing (TVD) Runge–Kutta scheme (Gottlieb and Shu, 1998).
Solitary waves, monochromatic waves, and spectral wave conditions can be generated using prescribed wave-maker boundary profiles, Dirichlet boundary conditions, or relaxation zones following Jacobsen et al. (2012). Similarly, outlet boundary conditions may include active wave absorption or relaxation zones.
The model incorporates a wetting–drying algorithm for wave run-up, based on a water-depth threshold controlling the dynamic extension of the computational domain. Bihs and Wang (2025) demonstrate that the combined shock-capturing and wetting–drying schemes reproduce experimental observations of wave breaking and run-up with good accuracy.
By solving the Euler equations and representing bathymetry and structures as no-flux boundaries, NHFLOW inherently captures wave reflection and diffraction processes. This capability was validated for the case of Mehamn Harbor, Norway, by Bihs and Wang (2025).
For further details on the numerical framework and its positioning relative to other wave models, the reader is referred to Bihs and Wang (2025).

2.3 *SWAN*

The third-generation, fully spectral wave model SWAN (Simulating WAves Nearshore; Booij et al., 1999) solves the wave-action balance equation (Eq. 4) for the wave-action density N(defined as $N = E/f$, where $E$is the wave energy density of a given wave component and $f$its intrinsic frequency) using a second-order finite-difference scheme:

$$\frac{\partial N}{\partial t} + \frac{\partial (c_g + u)_i N}{\partial x_i} + \frac{\partial c_f N}{\partial f} + \frac{\partial c_\theta N}{\partial \theta} = \frac{S_{tot}}{\sigma} \quad (4)$$

Wave action is advected in physical space by the group velocity c_g, and in the spectral domains of frequency f and direction θ by the propagation velocities c_f and c_θ, which primarily account for Doppler shifting and refraction, respectively. The term S_{tot} represents the sum of source and sink terms, including nonlinear wave–wave interactions, bottom friction, and wave breaking. Wind input is not considered in the present study.

Because SWAN is based on phase-averaged wave-action propagation, it allows the use of coarser spatial grids compared with phase-resolving models such as NHFLOW. However, the frequency and directional dimensions must be resolved as additional spectral coordinates. SWAN supports various grid types (e.g., curvilinear grids), although only rectilinear grids are employed in this work.
Wave spectra can be prescribed at the domain boundaries using Dirichlet boundary conditions. Beaches and sheltered domain boundaries without incoming wave energy are typically represented using free-propagation (Neumann-type) boundary conditions. Consequently, wave reflection is not inherently resolved in SWAN.
A phase-decoupled diffraction approximation was introduced by Holthuijsen et al. (2003), yielding reasonable results for idealised cases such as the Sommerfeld solution. In practical applications involving full frequency spectra, however, this approach is applicable only to obstacles with negligible reflection and is explicitly not recommended for large breakwaters or harbour configurations.

3 VALIDATION FOR THE SOMMERFELD SOLUTION

3.1 *Validation Methodology*

To reproduce the Sommerfeld solution numerically, a computational setup was developed to generate, propagate, and absorb

waves around a vertical, slender breakwater. The configuration is illustrated in Fig. 3. A relaxation-zone scheme is applied for both wave generation and absorption, effectively minimising reflections of incident, reflected, and diffracted waves. At the lateral boundaries not affected by diffracted waves, symmetry-plane (Cauchy-type) boundary conditions are imposed. A Cartesian grid is employed, with equal spatial discretisation in the horizontal directions (Δx = Δy). Due to grid constraints, the minimum feasible breakwater thickness of 3Δx is adopted.

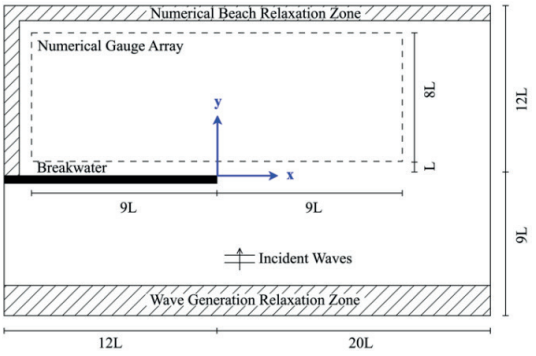

Figure 3. Numerical domain setup for the Sommerfeld validation case in NHFLOW (not to scale; dimensions relative to the incident wavelength L)

For wave generation, a monochromatic, long-crested incident wave field is prescribed with wave height $H = 0.2$ m and wavelength $L = 10$ m. Waves propagate over a constant still-water depth $d = 6$ m, ensuring deep-water conditions and preventing bottom effects from influencing the results. The incident wave height is verified in the fully developed region upstream of the breakwater using a numerical wave gauge positioned outside the reflection zone and analysed through a down-crossing method.

To compare the numerically obtained diffracted wave heights with the analytical Sommerfeld solution, an array of 37 × 9 numerical wave gauges is placed in the lee of the breakwater. The surface elevation time series are analysed using the down-crossing method, and the corresponding diffraction coefficients k_{diff} are computed and compared with analytical values at each gauge location.

The gauges are distributed along the x-axis in increments of 0.5L, spanning from $x = -9L$ to $x = 9L$, and centred about the y-axis. Along the y-axis, gauges are positioned from $y = 1L$ to $y = 9L$ in increments of 1L (see Fig. 3). Model performance is evaluated using the root-mean-square error (RMSE) of k_{diff} over the gauge array, as well as the mean relative deviation. Simulations are run for 240 s, and diffracted wave heights are extracted from $t = 210$ sonward to ensure a fully developed wave field.

The horizontal grid resolution is set to Δx = Δy = 0.15 m, and adaptive time stepping is applied with a Courant–Friedrichs–Lewy number of CFL = 0.5. To assess the sensitivity of the results to vertical resolution, additional simulations are conducted with varying numbers of grid layers in the vertical σ-coordinate. A hyperbolic stretching transformation is applied to the normalised σ-coordinates $\sigma_{i,\mathrm{norm}}$, mapping them to the physical vertical coordinate z_i between the seabed ($z = 0$) and the free surface ($z = d + \eta$), according to:

$$z_i = (d + \eta)\frac{\sinh[\xi(\sigma_{i,\mathrm{norm}} - 1)] + \sinh(\xi)}{\sinh(\xi)} \qquad (5)$$

where the stretching factor is set to $\xi = 2.5$.

3.2 *Validation Results*

The recreated Sommerfeld solution is simulated in NHFLOW using 3, 5, 7, 10, and 12 σ-layers. The resulting wave field obtained with 12 σ-layers is shown in Fig. 4. Table 1 summarises the mean relative deviation of the diffraction coefficients averaged over all 333 numerical gauges, $\Delta k_{\mathrm{diff,mean}}$, and the corresponding root-mean-square error, $\mathrm{RMSE}_{k_{\mathrm{diff}}}$.

While $\Delta k_{\mathrm{diff,mean}}$ is sensitive to the magnitude of the analytical diffraction coefficients (which decrease rapidly toward zero in the sheltered region lee of the breakwater), the RMSE provides a measure of the absolute accuracy of the reproduced wave heights in the numerical model.

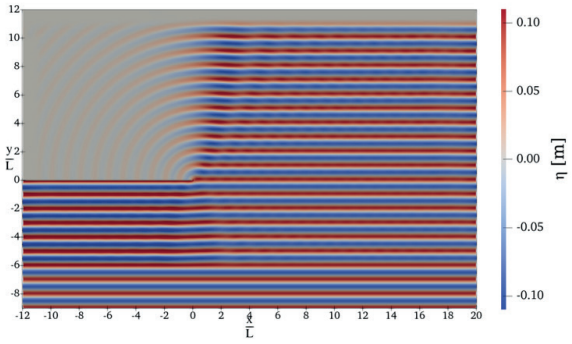

Figure 4. Water level elevation η in the Sommerfeld case as simulated with NHFLOW (12 σ-layers)

Table 1. Mean relative diffraction coefficient deviation $\Delta k_{\mathrm{diff,mean}}$ and root-mean-square error $\mathrm{RMSE}_{k_{\mathrm{diff}}}$ for different vertical resolutions.

σ-layers	$\Delta k_{\mathrm{diff,mean}}$ [%]	$\mathrm{RMSE}_{k\mathrm{diff}}$ [-]
3	11.82	0.0573
5	7.39	0.0187
7	6.51	0.0132
10	6.22	0.0120
12	6.14	0.0118

These results are illustrated in Fig. 5 and show continuous convergence with increasing numbers of σ-layers. The asymptotic behaviour is approximately quantified by applying a least-squares fit of a convergence function to $\Delta k_{\mathrm{diff,mean}}$ as a function of the normalised vertical grid spacing (inverse number of σ-layers). Following the procedure proposed by Eça and Hoekstra (2014), an approximate convergence order of 2.85 is obtained. Richardson extrapolation to an infinitely fine discretisation yields a projected residual value of $\Delta k_{\mathrm{diff,mean}} = 6.02\%$, with a 95% confidence interval range of 0.10 percentage points. The results obtained with 12 σ-layers lie marginally outside this narrow confidence interval and may therefore be considered sufficiently converged. The corresponding RMSE of k_{diff} is 0.012.

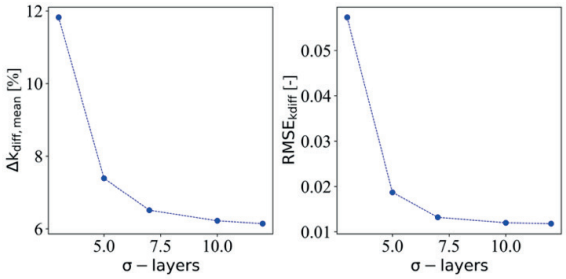

Figure 5. Mean relative diffraction coefficient deviation $\Delta k_{\mathrm{diff,mean}}$ and root-mean-square error $\mathrm{RMSE}_{k_{\mathrm{diff}}}$ as a function of vertical resolution

To assess the spatial reproduction of the diffraction coefficients and qualitatively evaluate the agreement, the individual gauge results are compared with the analytical Sommerfeld solution in Fig. 6.

The results demonstrate very good qualitative agreement with the spatial distribution predicted by the analytical solution. However, diffraction coefficients in the sheltered region (x < 0) are slightly underpredicted by the numerical model.

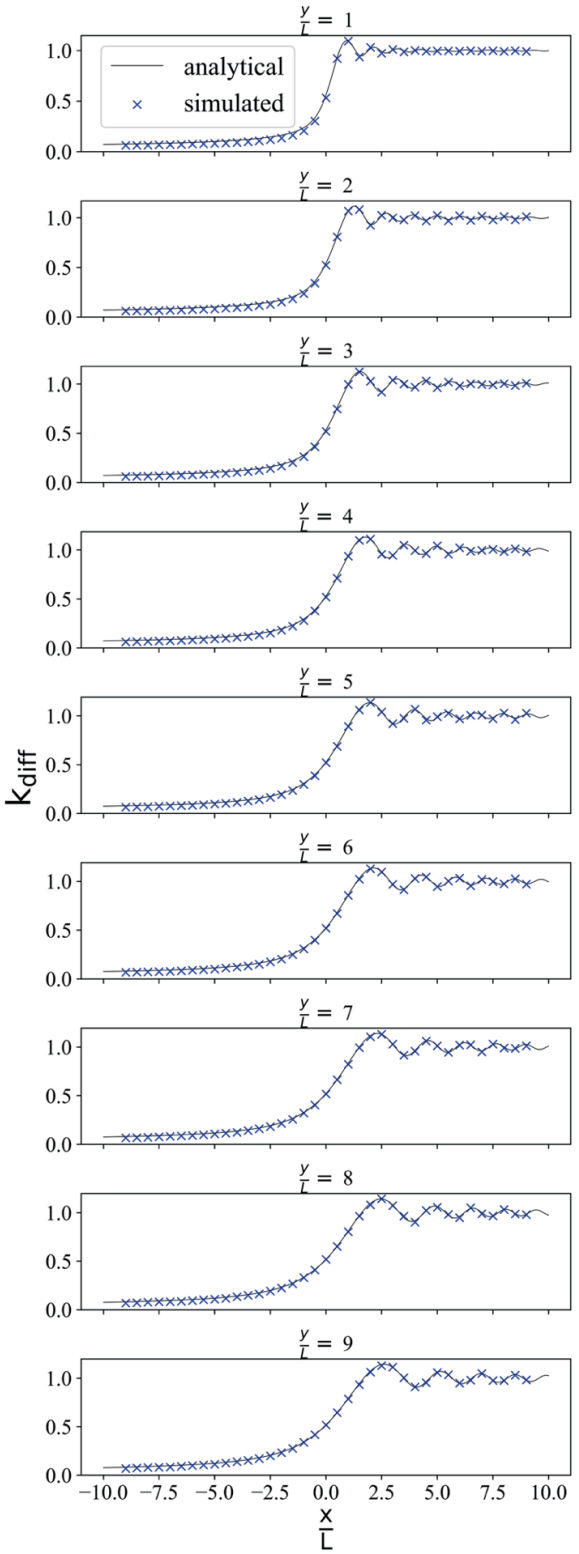

Figure 6. Diffraction coefficients k_{diff}at numerical wave gauges for 12 σ-layers (blue) compared with the analytical Sommerfeld solution (black)

The combination of a small RMSE and a comparatively larger $\Delta k_{\mathrm{diff,mean}}$ indicates that most of the relative error originates in the strongly sheltered region, where k_{diff} is small. To investigate this further, four subsets of the numerical gauge array (18 gauges each) are analysed individually for the 12-layer simulation. For both the sheltered region (x < 0) and the exposed region (x > 0) lee of the breakwater, gauges located at y = 1L and y = 9L are considered separately. The resulting values of $\Delta k_{\mathrm{diff,mean}}$ and $\mathrm{RMSE}_{k_{\mathrm{diff}}}$ are summarised in Table 2. The deviations from the analytical solution are larger in the sheltered region (x < 0), where wave energy results solely from diffraction under perpendicular wave incidence. In contrast, the exposed region (x > 0) is influenced by interference between incident, reflected, and diffracted waves (Penney and Price, 1952), resulting in smaller relative deviations.

Furthermore, gauges located farther from the breakwater tip (y = 9L) show closer agreement with the analytical solution than those closer to it (y = 1L). This behaviour is interpreted as a consequence of the geometric discrepancy between the analytical and numerical representations of the breakwater.

In the analytical model, the obstacle is infinitely thin and exhibits a mathematical singularity at its tip. In contrast, the numerical representation employs a finite breakwater thickness of 3Δx, and the singularity at the tip does not exist. The observed discrepancies are therefore attributed primarily to this geometric approximation rather than to deficiencies in the numerical wave propagation scheme.

Table 2. Mean relative diffraction coefficient deviations $\Delta k_{\mathrm{diff,mean}}$ and root-mean-square errors $\mathrm{RMSE}_{\mathrm{kdiff}}$ in the gauge subsets for 12 σ-layers

	$\Delta k_{\mathrm{diff,mean}}$ [%]		$\mathrm{RMSE}_{\mathrm{kdiff}}$ [-]	
	x < 0	**x > 0**	**x < 0**	**x > 0**
y = 1L	17.87	0.66	0.0222	0.0083
y = 9L	7.22	0.51	0.0090	0.0067

4 HARBOR APPLICATION CASE

4.1 *Modelling of Diffraction in Sirevåg Harbor with NHFLOW and SWAN*

To reproduce the bathymetry of Sirevåg Harbor in a numerical model, a digital elevation model (DEM) of the area was obtained from publicly available data provided by the Norwegian Mapping Authority (Kartverket). The dataset was further processed by manually correcting missing elevation values above the shoreline. The emerged sections of the main breakwater protecting the harbor were manually reconstructed based on the cross-sectional specifications reported by Sigurdarson et al. (2003), with particular attention to berm slopes and crest elevations.

To define the input wave spectrum, spectral hindcast data from the nearest offshore grid point (lon: 5.7608°, lat: 58.4902°) in NORA3 (Norwegian Reanalysis Archive 3), provided by the Norwegian Meteorological Institute (Haakenstad et al., 2021; Breivik et al., 2022), were analysed for the period between May 2023 and May 2024 to identify the most extreme sea state. The selected extreme conditions are: Significant wave height: $H_s = 7.13$m; Peak period: $T_p = 14.86$s; Mean wave direction: $\theta_m = 294.95°$(nautical convention)

The water level is set to mean sea level, and tidal effects as well as storm surge are neglected. Although this simplification would influence results in a full risk-assessment context, it is considered acceptable here for the purpose of comparing wave propagation and diffraction patterns simulated by the two models.

The selected sea state is simulated in both NHFLOW and SWAN using a rotated computational domain of 2120 m × 2070 m, oriented such that θ_m is aligned with the x-axis (Fig. 7). A uniform horizontal grid with $\Delta x = \Delta y = 5$m is applied in both models.

In NHFLOW, five σ-layers are used for vertical discretisation, with hyperbolic stretching applied as described in Section 3.1.

Six numerical wave gauges are placed at identical locations in both models (see Fig. 7 and Table 3). These positions are selected to sample: (1) Incident wave conditions offshore; (2) Propagated wave conditions approaching the harbor; (3) Wave conditions near the breakwater head at the harbor entrance; (4) The lee side of the main breakwater; (5) The first harbor basin; (6) The marina area at the rear of the second harbor basin, separated by a secondary breakwater

In both models, wave boundary conditions are prescribed only at the offshore boundary (x = 0 m). In NHFLOW, this is implemented via a relaxation zone. Absorption relaxation zones are applied at the lateral boundaries.

In SWAN, free-propagation (radiation) boundary conditions are imposed at the lateral boundaries.

A total simulation time of 12,600 s is performed in NHFLOW. The frequency spectrum at each gauge location is reconstructed using a Fast Fourier Transform (FFT), and significant wave heights H_s are computed from the zero-moment wave height. A spin-up period of 1,800 s is allowed for the development of the wave field

before sampling the free-surface elevation $\eta$for spectral analysis.
In SWAN, the spectrum is imposed as a stationary boundary condition. Consequently, the model is executed in stationary mode (i.e. the unsteady term $\partial N / \partial t$ in Eq. 4 is omitted).
In SWAN, H_s is extracted directly from the spectral solution at each grid point. The spatial distributions of $H_s$are plotted over the full domain for qualitative comparison between the models.
At gauge position 1, the simulated spectra from both models are matched by fitting to a JONSWAP spectrum (following Goda, 1988) to ensure comparable incident wave conditions. This step is necessary because the extreme wave parameters are expected to interact nonlinearly with the relatively shallow bathymetry.
At the remaining gauge positions, the computed H_s values from NHFLOW and SWAN are compared quantitatively to assess differences in simulated wave propagation and diffraction into the harbor.

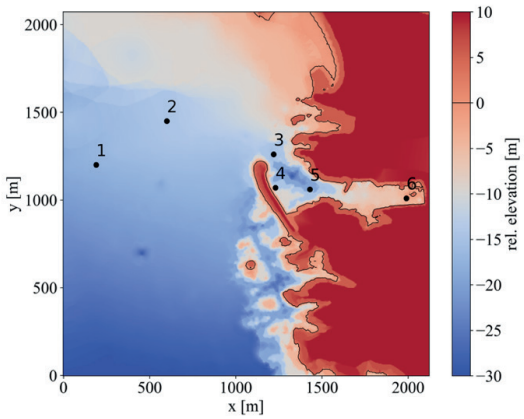

Figure 7. Computational domain showing bathymetry relative to still water level (0 m, positive upward) and the six numerical wave gauge locations

4.2 *Model Comparison in the Harbor Application Case*

Analysis of the simulated time series at the incident wave gauge (Gauge 1; see Fig. 7) in NHFLOW yields a JONSWAP spectrum with $H_s = 5.82\text{m}$ and $T_p = 14.86\text{s}$. The fully developed wave field is shown in Fig. 8, and the spatial distribution of significant wave heights over the full computational domain is presented in Fig. 9.
The same spectral parameters are imposed in SWAN, achieving a parameter convergence greater than 99.5%. The resulting significant wave heights are shown in Fig. 10. For improved comparison of wave conditions within the harbor, close-up views of the significant wave height distributions are provided in Fig. 11 (NHFLOW) and Fig. 12 (SWAN).

Table 3 lists the significant wave heights at the six gauge locations (see Fig. 7), allowing for quantitative comparison between the two models. The domain-wide significant wave height distributions show broadly similar large-scale behaviour in both models. In both cases, wave refraction over the bathymetry results in convergence and divergence patterns toward the shoreline. However, clear differences in wave-field representation are evident. NHFLOW exhibits standing wave patterns near solid boundaries and along the shoreline, whereas SWAN produces characteristic wave-ray patterns. These differences are also apparent at the breakwater opening and within the harbor basins.
At Gauge 2, substantial differences arise in the predicted wave propagation toward the shoreline. NHFLOW predicts considerably less wave energy at this location compared to SWAN. This discrepancy may be related to differences in the treatment of refraction and wave attenuation processes (e.g. depth-induced breaking and whitecapping) in SWAN, compared with the phase-resolved, shock-capturing formulation in NHFLOW. The effect is particularly pronounced because Gauge 2 is located near a zone of wave divergence. A similar trend is observed at Gauge 3, near the breakwater opening, where SWAN predicts higher wave energy than NHFLOW.
Despite these differences offshore of the breakwater, the models' treatment of diffraction becomes critical inside the harbor. Significant wave heights predicted in the lee of the breakwater (Gauges 4–6) are substantially higher in NHFLOW than in SWAN. In the first harbor basin (Gauge 5), the ratio between NHFLOW and SWAN results is approximately 2.3. In the second basin (Gauge 6), the ratio increases to 16.3.
These differences are consistent with the fact that diffraction-driven wave energy propagation is not accurately represented in SWAN. As shown in Fig. 12, the spectral model produces wave-energy rays inside the harbor similar to those in the refraction-dominated nearshore zone. These rays diverge toward the harbor walls, where energy is effectively dissipated due to the absence of wave reflection in the model formulation. The small amount of wave energy reaching the innermost harbor basin (Gauge 6) may result from minor ray penetration combined with numerical dispersion effects (cf. Holthuijsen et al., 2003).
In contrast, NHFLOW (Fig. 11) produces a smoother and more physically consistent distribution of wave energy within the harbor basins, including standing wave patterns generated by reflection and diffraction at structural boundaries. This results in significantly

higher and more conservative wave height predictions in sheltered areas.

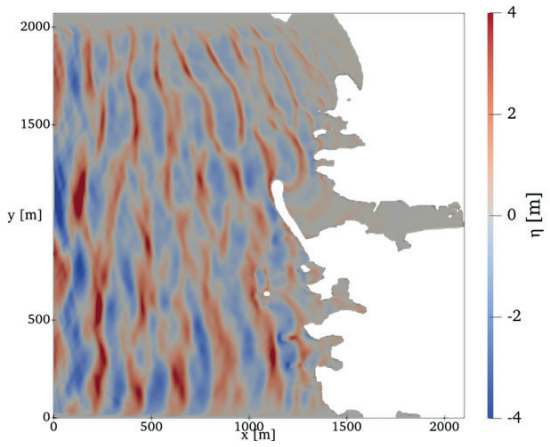

Figure 8. Water surface elevation η simulated with NHFLOW for the Sirevåg harbor case (t = 5400s)

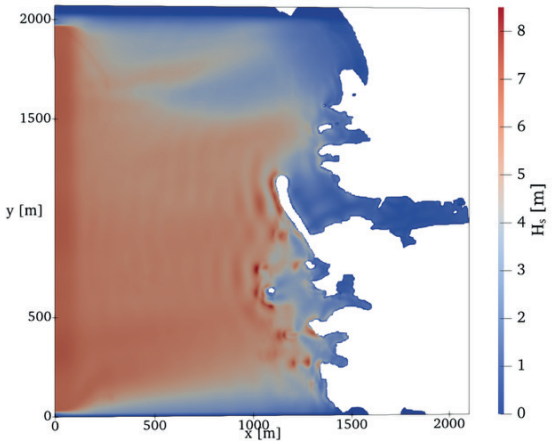

Figure 9. Significant wave heights H_s simulated with NHFLOW for the Sirevåg harbor case (FFT over 3 hours)

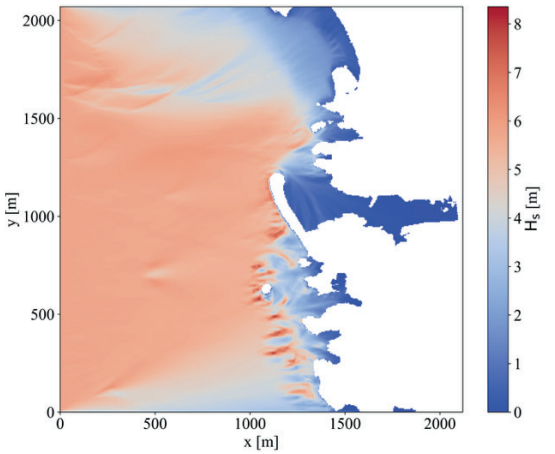

Figure 10. Significant wave heights H_s simulated with SWAN for the Sirevåg harbor case (stationary model)

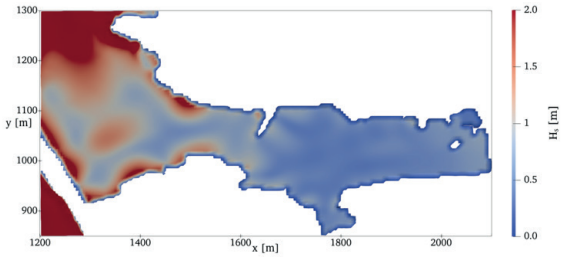

Figure 11. Harbor close-up of significant wave heights H_s simulated with NHFLOW (FFT over 3 hours)

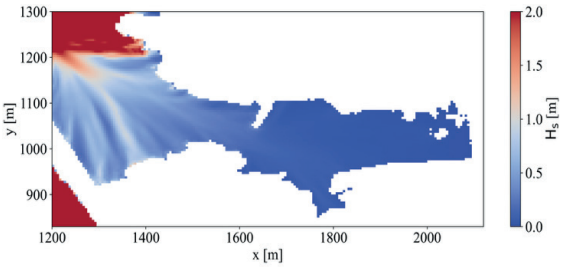

Figure 12. Harbor close-up of significant wave heights H_s simulated with SWAN (stationary solution)

Table 3. Wave gauge coordinates and significant wave heights H_s in NHFLOW and SWAN (relative difference expressed as SWAN vs. NHFLOW)

Gauge No.	Pos x [m]	Pos y [m]	H_s NHFLOW [m]	H_s SWAN [m]	Relative Difference [%]
1	190	1200	5.82	5.82	0
2	600	1450	4.96	5.48	+10.48
3	1220	1260	2.56	3.06	+19.53
4	1230	1070	1.28	0.48	–62.50
5	1430	1060	0.75	0.32	–57.33
6	1990	1010	0.49	0.03	–93.88

5 CONCLUSIONS

Although an infinitely thin obstacle cannot presently be represented exactly in NHFLOW, the model reproduces the Sommerfeld solution of Penney and Price (1952) with high accuracy. An RMSE of 0.012 for the diffraction coefficients in the lee of a slender breakwater is achieved (using high vertical resolution) relative to the analytical solution. Most of the relative error occurs at locations where the diffraction coefficients are small, i.e. in strongly sheltered regions.

A practical application of diffraction modelling with NHFLOW is demonstrated for the Sirevåg harbor case. When matched wave spectra are imposed, NHFLOW predicts less wave energy

reaching the breakwater opening compared to the spectral wave model SWAN. However, the significant wave heights within the harbor basins are substantially higher in NHFLOW, and the resulting wave patterns exhibit more physically consistent spatial distributions than those obtained with SWAN. These findings indicate that the phase-resolving model NHFLOW provides more conservative and physically realistic predictions of wave conditions inside sheltered harbor areas.

Overall, this study demonstrates the high accuracy of REEF3D::NHFLOW in modelling diffraction processes and highlights its capability to resolve combined refraction–diffraction–reflection interactions in wave propagation toward and within harbor environments.

ACKNOWLEDGEMENTS

The authors acknowledge funding from the European Union (ERC, PARTRES, 101045646). The views and opinions expressed are those of the authors only and do not necessarily reflect those of the European Union or the European Research Council Executive Agency. Neither the European Union nor the granting authority can be held responsible for them.

The simulations were performed on the supercomputer Betzy, provided by Sigma2 – the National Infrastructure for High-Performance Computing and Data Storage in Norway.

REFERENCES

Bihs, H., Ehlers, R., Wang, W. (2024). A shock-absorbing non-hydrostatic navier-stokes solver on σ-grids for wave modeling over irregular topography. *OMAE 43 proceedings vol. 6*

Bihs, H., Kamath, A., Alagan Chella, M., Aggarwal, A., Arntsen, Ø.A. (2016). A new level set numerical wave tank with improved density interpolation for complex wave hydrodynamics. *Computers & Fluids 140*: 191–208.

Bihs, H., Wang, W.W. (2025). REEF3D::NHFLOW–A high-performance non-hydrostatic solver for coastal wave propagation. *Coastal Engineering 202*.

Booij, N., Ris, R.C., Holthuijsen, L.H. (1999). A third-generation wave model for coastal regions: 1. model description and validation. *J. Geophys. Res. 104*: 7649–7666.

Breivik, Ø., Carrasco, A., Haakenstad, H., Aarnes, O.J., Behrens, A., Bidlot, J., Björkqvist, J., Bohlinger, P., Furevik, B.R., Staneva, J., Reistad, M. (2022). The impact of a reduced high-wind Charnock parameter on wave growth with application to the North Sea, the Norwegian Sea, and the Arctic Ocean. *JGR Oceans 127*.

Carr, J.H., Stelzriede, M.E. (1952). Diffraction of water waves by breakwaters. *U.S. Nat. Bur. Stds 521*: 109–125.

Dean, R.G., Dalrymple, R.A. (1991). Water Wave Mechanics for Engineers and Scientists, 2nd ed. World Scientific.

Eça, L., Hoekstra, M. (2014). A procedure for the estimation of the numerical uncertainty of CFD calculations based on grid refinement studies. *Journal of Computational Physics 262: 104–130*.

Fresnel, A.-J. (1819). Mémoire sur la diffraction de la lumière [Memoir on the diffraction of light]. *Mémoires de l'Académie des Sciences de l'Institut de France 5*: 339–475.

Goda, Y. (1988). Statistical variability of sea state parameters as a function of wave spectrum. *Coastal Engineering in Japan 31*: 39–52.

Goda, Y. (2000). Random seas and design of maritime structures, 2nd ed. World Scientific.

Gottlieb, S., Shu, C.-W. (1998). Total variation diminishing Runge-Kutta schemes. *Math. Comp. 67*: 73–85.

Haakenstad, H., Breivik, Ø., Furevik, B.R., Reistad, M., Bohlinger, P., Aarnes, O.J. (2021). NORA3: A nonhydrostatic high-resolution hindcast of the North Sea, the Norwegian Sea, and the Barents Sea. *Journal of Applied Meteorology and Climatology 60*: 1443–1464.

Holthuijsen, L.H., Herman, A., Booij, N. (2003). Phase-decoupled refraction–diffraction for spectral wave models. *Coastal Engineering 49*: 291–305.

Huygens, C. (1690). Traité de la lumière [Treatise on light]. Chez Pierre van der Aa.

Jacobsen, N.G., Fuhrman, D.R., Fredsøe, J. (2012). A wave generation toolbox for the open-source CFD library: OpenFoam®. *Numerical Methods in Fluids 70*:1073–1088.

Jiang, G.-S., Shu, C.-W. (1996). Efficient implementation of weighted ENO schemes. *Journal of Computational Physics 126*: 202–228.

Kartverket. Norwegian national elevation model [Høydedata]. Retrieved April 17, 2025.

Morse, P.M., Rubenstein, P.J. (1938). The Diffraction of Waves by Ribbons and by Slits. *Phys. Rev. 54*: 895–898.

Norwegian Meteorological Institute. NORA3 - Norwegian reanalysis archive 3 [nora3_wave]. Retrieved March 25, 2025.

Penney, W.G., Price, A.T. (1952). Part I: The diffraction theory of sea waves and the shelter afforded by breakwaters. *Phil. Trans. R. Soc. Lond. A 244*: 236–253.

Sieger, B. (1908). Die Beugung einer ebenen electrischen Welle an einem Schirm von elliptischem Querschnit [Diffraction of a plane electric wave at a screen with eliptic cross section]. *Ann. Phys. 27*: 626–664.

Sigurdarson, S., Jacobsen, A., Smarason, O.B., Bjørdar, S., Viggosson, G., Urrang, C., Tørum, A. (2004). Sirevåg berm breakwater, design, construction and experience after design storm. *Coastal Structures 2003 proceedings*: 1212–1224.

Sommerfeld, A. (1896). Mathematische Theorie der Diffraction [Mathematical theory of diffraction]. *Math. Ann. 47*: 317–374.

United States Army Corps of Engineers (2008). Coastal engineering manual part II: Coastal hydrodynamics. U.S. Dept. of Transportation.

Wang, W., Martin, T., Kamath, A., Bihs, H. (2020). An improved depth-averaged nonhydrostatic shallow water model with quadratic pressure approximation. *Numerical Methods in Fluids 92*: 803–824.
Wang, W., Pákozdi, C., Kamath, A., Fouques, S., Bihs, H. (2022). A flexible fully nonlinear potential flow model for wave propagation over the complex topography of the Norwegian coast. *Applied Ocean Research 122*: 103103.